

# Lagrangian barriers to heat transport in turbulent three-dimensional convection

Philipp P. Vieweg,<sup>1</sup> Christiane Schneide,<sup>2</sup> Kathrin Padberg-Gehle,<sup>2</sup> and Jörg Schumacher<sup>1</sup>

<sup>1</sup>*Institut für Thermo- und Fluidodynamik, Technische Universität Ilmenau, Postfach 100565, D-98684 Ilmenau, Germany*

<sup>2</sup>*Institut für Mathematik und ihre Didaktik, Leuphana Universität Lüneburg, D-21335 Lüneburg, Germany*

(Dated: May 25, 2022)

Barriers to the turbulent transport of heat in a convection flow can be identified by Lagrangian trajectories that stay together for a long time and thus probe spatial regions in the bulk of the fluid flow that do not mix effectively with its surroundings. They form Lagrangian coherent sets which we investigate here in direct numerical simulations of three-dimensional Rayleigh-Bénard convection at three different Prandtl numbers. The analysis is based on 524,288 massless Lagrangian tracer particles which are advected in the time-dependent flow. Clusters of trajectories are identified by the diffusion map approach, which quantifies the connectivity of trajectory segments by a diffusion process on the data, and a subsequent sparse eigenbasis approximation (SEBA) for cluster detection. The diffusion kernel contains a cutoff that is based on the time-averaged distance between mutual Lagrangian tracers in a time window. The numerical simulations are performed in a cell at an aspect ratio  $\Gamma = 16$ , at fixed Rayleigh number  $Ra = 10^5$ , and Prandtl numbers  $Pr = 0.1, 0.7$  and  $7$ . The combination of diffusion map and SEBA leads to a significantly improved cluster identification that is compared with the large-scale patterns in the Eulerian frame of reference. We show that the Lagrangian coherent sets contribute significantly less to the global turbulent heat transfer for all chosen Prandtl numbers as the trajectories in the spatial complement. This is realized by monitoring local Nusselt numbers, a dimensionless measure of heat transfer, along the tracer trajectories.

PACS numbers:

## I. INTRODUCTION

The investigation of transport and mixing properties in complex dynamical systems in the Lagrangian frame of reference has received an increasing interest in the past two decades and many different identification methods have been developed and applied to fluid flow, see [1–3] for recent reviews. Central to these approaches is the concept of a Lagrangian *coherent set* (CS) [1, 4–6], a region in the fluid volume that only weakly mixes with its surrounding and which often stays regularly shaped (non-filamented) under the evolution by the flow. Coherent sets were originally introduced based on transfer operators [4, 5], but in the past few years several approaches were proposed that use spatio-temporal clustering algorithms applied to Lagrangian trajectory data [7–13]. These algorithms aim at identifying coherent sets as groups of trajectories that remain close to each other or behave in a similar manner in the time interval under investigation. In turbulent convection flows, the heat transport from the bottom to the top across an extended layer or a closed vessel is one of the essential processes that require a deeper understanding [16, 17] in view to the numerous geophysical [18], astrophysical [19] and technological [20] applications. One first step is to identify the spatial sets that contribute least to this transport – and thus can be considered as barriers of the transport – and to relate them to the large-scale structures which are observed in the Eulerian frame of reference.

In the present work, we identify the Lagrangian coherent sets as barriers to the turbulent heat transfer in a three-dimensional Rayleigh-Bénard convection (RBC) flow in a layer between two parallel plates that is uniformly heated from below and cooled from above. Our Lagrangian analysis of turbulent RBC is based on a diffusion map approach [9, 21, 22] and will be conducted for three different Prandtl numbers  $Pr$ , a dimensionless parameter that relates the viscosity of the fluid to its temperature diffusivity and thus varies for different working fluids. To extract Lagrangian coherent sets from spectral properties of the diffusion map, we apply the recently developed sparse eigenbasis approximation (SEBA) [23]. The combination of these methods allows us to disentangle the contribution of the tracer trajectories that are trapped in Lagrangian coherent sets to the overall heat transfer in comparison to the rest, extending our recent Lagrangian studies of RBC [13–15] to the analysis of turbulent transport. Figure 1 illustrates these coherent sets in panel (a) in a perspective view and replots representative trajectories in panel (b). These regions will be identified as the ones that contribute least to the turbulent heat transfer by a monitoring of the local Nusselt number along individual Lagrangian trajectories segments.

## II. DIRECT NUMERICAL SIMULATIONS

The three-dimensional equations of motion are solved numerically in the Boussinesq approximation by the spectral element method nek5000 [13, 24, 25]. Details of all simulations are summarized in Table I. The equations are made dimensionless by the following quantities: layer height  $H$ , wall-to-wall temperature difference  $\Delta T$ , and free-fall velocity

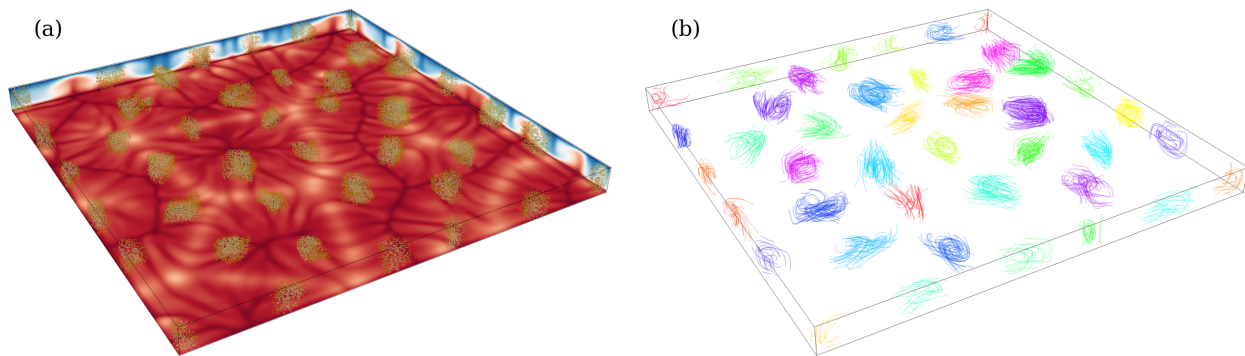


FIG. 1: Visualization of Lagrangian coherent sets. (a) The 40,049 Lagrangian tracers which correspond to Lagrangian coherent sets are shown for  $Ra = 10^5$ ,  $Pr = 7$ , and  $\Gamma = 16$  (Run 3). The color of each Lagrangian tracer indicates the probability to belong to one of the coherent subsets. These particles comprise the cluster cores during the chosen time interval  $[t_0, t_0 + \Delta t]$  with  $\Delta t = 17$ , while the exact tracer positions correspond  $t_0 + \Delta t/2$ . Three cell faces display contours of the temperature field averaged over the same time interval. The bottom plane is at  $z = 0.05$ . (b) A representative subset of 1,600 Lagrangian trajectories is shown that form the different clusters for the same time interval as panel (a). Different colors indicate different clusters.

$U_f = \sqrt{g\alpha\Delta TH}$  with the acceleration due to gravity  $g$  and the isobaric expansion coefficient  $\alpha$ . This results to

$$\nabla \cdot \mathbf{u} = 0, \quad (1)$$

$$\frac{\partial \mathbf{u}}{\partial t} + (\mathbf{u} \cdot \nabla) \mathbf{u} = -\nabla p + \sqrt{\frac{Pr}{Ra}} \nabla^2 \mathbf{u} + T \mathbf{e}_z, \quad (2)$$

$$\frac{\partial T}{\partial t} + (\mathbf{u} \cdot \nabla) T = \frac{1}{\sqrt{RaPr}} \nabla^2 T. \quad (3)$$

We consider a closed cell with square horizontal cross section  $L_{\text{hor}} \times L_{\text{hor}}$  and an aspect ratio of  $\Gamma = L_{\text{hor}}/H = 16$ . No-slip boundary conditions for the velocity field are applied at all walls. The sidewalls are thermally insulated and  $T_{\text{bottom}} = 1$  and  $T_{\text{top}} = 0$  are chosen. The volume is covered by more than 440,000 spectral elements and the turbulence fields are expanded with respect to higher-order polynomials in each spatial direction and on each spectral element. The Rayleigh number is given by  $Ra = g\alpha\Delta TH^3/(\nu\kappa) = 10^5$  and the Prandtl number  $Pr = \nu/\kappa$  (see Table I). Here,  $\nu$  is the kinematic viscosity and  $\kappa$  is the thermal diffusivity. We advect  $N = 524,288$  massless Lagrangian tracer particles by  $\dot{\mathbf{X}}_i = \mathbf{u}(\mathbf{X}_i, t)$  for  $i = 1, \dots, N$ . Interpolation of fields on the tracer position can be done spectrally in the present method, implying that the interpolation procedure is as accurate as the simulation itself. The cluster analysis starts when the Lagrangian tracer particles are uniformly distributed across the cell after initial seeding.

It is known that turbulent convection flows in extended domains get organized into prominent large-scale patterns which are termed turbulent superstructures of convection, see e.g. [26–30]. Table I compares the characteristic lengths and times for the Eulerian ( $E$ ) and Lagrangian ( $L$ ) frames (for comparison see also refs. [13, 27]). The Eulerian characteristic length  $\bar{\lambda}^E$  is the wavelength that corresponds to the wavenumber  $k^*$  at which the time-averaged Fourier spectrum of the vertical velocity component in the midplane becomes maximal. The Eulerian characteristic time is a mean turnover time calculated by  $\bar{\tau}^E \approx \pi(\lambda^E + 2)/(4u_{\text{rms}})$ . The corresponding Lagrangian values are obtained as means of the probability density functions (PDFs) which are taken over the whole tracer ensemble. Therefore, we take  $\lambda^L$  as four times the horizontal travel distance of each tracer between two successive intersections of the midplane (this distance probes basically the typical double counterrotating roll structure on average). In comparison  $\tau^L$  is the time each particle needs to complete a full turnover, which is probed by passing the heights  $z = 0.2$  and  $0.8$ . In spite of the fat tails of all distributions, the mean values are found to be close to the corresponding characteristic scales of the Eulerian frame which confirms the consistency of our analyses.

### III. SPECTRAL ANALYSIS OF DIFFUSION MAP AND SEBA CLUSTERING

Material transport is subject to turbulent dispersion which will destroy Lagrangian coherence if one only waits long enough. We aim to identify subsets of our  $N$  Lagrangian trajectories that stay close together for a longer transient period  $\Delta t$ . To this end, we define a diffusion process on the discrete data and explore internal connectivities. This is known as the *diffusion map approach* [21, 22], which was recently extended to CS analyses [9]. We use a time-averaged

Run	Ra	Pr	$\text{Nu}^E$	$\bar{\tau}^E$	$\bar{\lambda}^E$	$\Delta t^L$	$\bar{\tau}^L$	$\bar{\lambda}^L$	$\epsilon$	$\Delta t$	$N_{\text{CS}}$	$\text{Nu}_{\text{CS}}^L$	$\text{Nu}_{\text{RP}}^L$	$\xi_p$	$\xi_q$
1	$10^5$	0.1	3.50	10.6	3.4	133	$13.7 \pm 8.7$	$3.7 \pm 2.1$	49/800	3.25	75	2.89	3.54	7.6%	6.3%
2	$10^5$	0.7	4.13	18.3	3.6	234	$21.7 \pm 14.5$	$3.6 \pm 2.1$	9/200	5.50	80	2.71	4.40	8.5%	5.4%
3	$10^5$	7.0	4.18	63.4	5.1	700	$68.6 \pm 51.1$	$5.0 \pm 2.4$	9/200	17.00	40	2.94	4.29	7.4%	5.2%

TABLE I: Parameters and global statistical measures of the simulations. The Rayleigh number Ra, the Prandtl number Pr, the global Nusselt number  $\text{Nu}^E = 1 + \sqrt{\text{RaPr}\langle u_z T \rangle_{V,t}}$ , the characteristic turnover time  $\bar{\tau}^E$  in the Eulerian (superscript  $E$ ) frame of reference, the characteristic turnover length  $\bar{\lambda}^E$  in the Eulerian frame obtained from the peak of the Fourier spectrum of the vertical velocity component at midplane, the total time of Lagrangian (superscript  $L$ ) analysis  $\Delta t^L$ , the mean Lagrangian turnover time  $\bar{\tau}^L$  and the mean Lagrangian turnover length  $\bar{\lambda}^L$  are listed. Furthermore, we list the kernel scale  $\epsilon$  of the diffusion map, the width  $\Delta t$  of each time window used to compute the time-averaged distance  $r_{ij}$ , the approximate number of detected Lagrangian coherent sets  $N_{\text{CS}}$ , the average Nusselt number related to the transport across the coherent sets  $\text{Nu}_{\text{CS}}^L$  as well as of the complement (remaining particles)  $\text{Nu}_{\text{RP}}^L$ , the mean fraction of Lagrangian particles in the coherent sets  $\xi_p$ , as well as the mean fraction of heat transported by them  $\xi_q$  for each simulation run. Uncertainties represent standard deviations. Times are given in units of the free-fall time  $T_f = H/U_f$ , lengths in units of  $H$ .

distance

$$r_{ij}(t_0) = \langle |\mathbf{X}_i(t_0) - \mathbf{X}_j(t_0)| \rangle_{\Delta t} \quad (4)$$

between mutual Lagrangian trajectories  $\mathbf{X}_i(t)$  and  $\mathbf{X}_j(t)$  with the time average  $\langle \cdot \rangle_{\Delta t}$  taken from  $t_0$  to  $t_0 + \Delta t$ . The corresponding graph Laplacian  $N \times N$  matrix is given by

$$L_{ij} = \frac{1}{\epsilon} (P_{ij} - \delta_{ij}). \quad (5)$$

This definition contains the kernel scale  $\epsilon$  which has to be chosen on physical grounds as discussed later.  $P_{ij}$  is the diffusion matrix constructed from the end points of the trajectories. In a nutshell, the component  $P_{ij}$  encodes the probability of hopping from Lagrangian trajectory endpoint  $i$  to  $j$ . The matrix  $L_{ij}$  thus generates a random walk on our trajectory data points. It can be rigorously shown that  $L_{ij}$  converges for the joint limit of  $N \rightarrow \infty$  and  $\epsilon \rightarrow 0$  to a Laplacian operator which describes a diffusion process and thus can explore the internal geometry of the data set [22], i.e., the trajectory clusters in our case [9].  $P_{ij}$  contains the time-averaged distance (4) as follows,

$$P_{ij} = \frac{\hat{K}_{ij}}{\sum_{j=1}^N \hat{K}_{ij}} \quad \text{with} \quad \hat{K}_{ij} = \frac{K_{ij}}{k_\epsilon(\mathbf{X}_i)k_\epsilon(\mathbf{X}_j)} \quad \text{and} \quad K_{ij} = \begin{cases} \exp(-r_{ij}^2/\epsilon), & r_{ij} \leq \delta \\ 0, & r_{ij} > \delta \end{cases}. \quad (6)$$

Here,  $\delta = \sqrt{2\epsilon}$  is the cut-off and  $k_\epsilon = \sum_{j=1}^N K_{ij}$  stands for pre-normalization. The matrix  $K_{ij}$  is a diffusion kernel matrix. Note that even though we work with a very large number of tracer particles, which in turn means that these matrices have  $(2 \times 512^2)^2 \approx 10^{11}$  entries, the sparsification in  $K_{ij}$  in (6) leads to densities below 1 percent and allows to use very efficient algorithms such as k-d tree data structures with no loss of accuracy [32]. Following Shi and Mailk [34] the following eigenvalue problem for the graph Laplacian has to be solved

$$L_{ij}v_j = \lambda^{(j)}v_j, \quad (7)$$

with the eigenvalues  $\lambda^{(j)}$  and corresponding eigenvectors  $v_j$ . Gaps in the spectrum indicate how to divide the graph into clusters, as also discussed in refs. [9, 13, 14, 23].

The connectivity of the graph depends on the kernel scale  $\epsilon$ , the time window  $\Delta t$ , and the number of Lagrangian trajectories  $N$ . While  $N$  is left unchanged, we found in prior parameter studies that  $\Delta t \approx 0.25\bar{\tau}^L$  with a kernel scale  $\epsilon$  as small as possible, gives the best results. The kernel scale depends on the Prandtl number (see Table I). At a given Rayleigh number, a decrease of Pr generates turbulence with a larger Reynolds number which in turn will cause a stronger dispersion. Thus  $\epsilon$  is larger in Run 1.

The leading  $N_l$  eigenvalues with  $N_l = 250 \ll N$  for 10 disjoint time intervals in each of the three runs are always computed, while about 50 equally spaced simulation snapshots are used to evaluate the time-averaged distances  $r_{ij}$  in each time window as given in (4). A typical spectrum is shown Fig. 2. A discretized version of the following relation is applied to detect the strongest gaps in the spectrum which are indicated by the grey bars in the figure ( $i > 5, i \leq N_l - 4$ ),

$$\chi_i = \frac{8G_i}{\sum_{k=1}^4 (G_{i-k} + G_{i+k})} - 1 \quad \text{with} \quad G_i = \left. \frac{\partial \lambda}{\partial n} \right|_i. \quad (8)$$

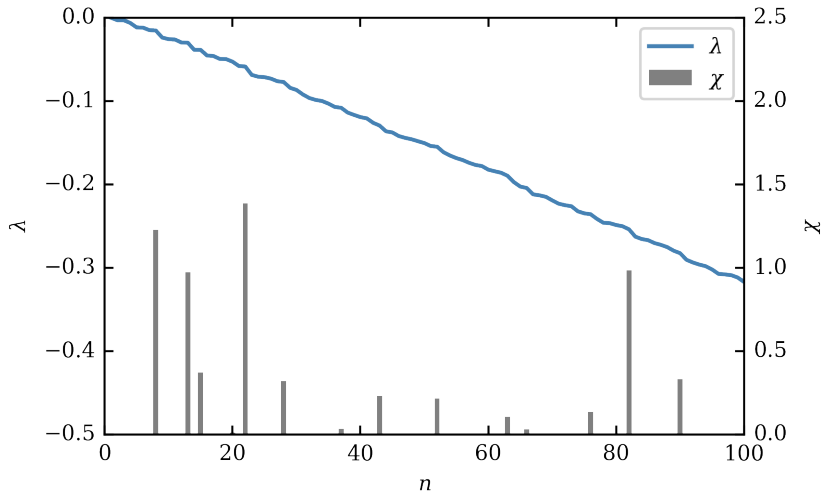


FIG. 2: A typical eigenspectrum (from top downwards) resulting for the graph Laplacian matrix  $L_{ij}$  which emerges from a diffusion map ansatz, here applied to Run 2. To highlight gaps from two subsequent eigenvalues  $\lambda$ , relation (9) is used.

The number of coherent sets  $N_{CS}$  can be estimated based on the aspect ratio of the cell and the Lagrangian length scale from Table I. This leads for example in Run 2 to  $N_{CS} \approx 80$  which is close to the peak at  $n = 82$  and demonstrates that this procedure can identify spectral gaps more objectively.

The key idea of SEBA is to transform the set of eigenvectors  $\{v_j\}_{j=1\dots N_i}$  to a new sparse eigenbasis of vectors  $\{z_k\}_{k=1\dots N_i}$  which spans the same subspace, such that the encoded connectivity of the graph after solving the eigenvalue problem is disentangled. Different sparse eigenbasis vectors represent then different features of the graph, and the entries can be interpreted as probabilities of a certain data point to belong to this particular feature [23]. By applying thresholds  $0 \leq \zeta \leq 1$  it is possible to filter out data points which do not exceed a certain likelihood of cluster affiliation. As a consequence, one obtains a number of features (or clusters) and a group of remaining data points. This is a clear improvement in comparison to the k-means method which was applied in our previous work [13].

Figure 3 displays the result of SEBA for the same data as in Fig. 2. Panel (a) indicates that the whole domain is covered by high feature likelihoods (in yellow). Thresholding these likelihoods in order to separate the features is shown in panel (b). These are the different Lagrangian coherent sets. Furthermore, these Lagrangian CS intersect in almost all cases the isotherm of mean temperature of  $\langle T \rangle_{\Delta t} = 0.5$ . This implies that these sets represent the core regions of the large-scale circulation rolls which make up the turbulent superstructures in convection. In (c) we replot Lagrangian CS now with a higher threshold of  $\zeta = 0.94$  for comparison which is used for the remainder of this work.

#### IV. BARRIERS TO TURBULENT HEAT TRANSPORT

Figure 4 confirms that the detected features indeed represent the core of convection rolls by providing the spatial distribution of the Lagrangian particles that belong to the coherent sets and comparing them with the remaining ones (RP) outside the identified sets. We display therefore the PDF of the vertical coordinate in panel (a) of the figure. The PDFs of the local temperature that carries each Lagrangian tracer are shown in addition in panels (b,c) in Fig. 4. All three Prandtl numbers display clearly a narrower distribution around  $\langle T \rangle_{\Delta t} = 0.5$  for the tracers in the CS which indicates that they are much less efficient in taking up and releasing the heat as those tracers outside the CS. The PDFs of  $T$  are broadest for the smallest Prandtl number as the diffusion time is shortest [27].

This suggests a closer look at the turbulent heat transport. The global heat transfer is given by  $\text{Nu}^E = 1 + \sqrt{\text{RaPr}} \langle u_z T \rangle_{V,t}$  and listed in Table I. We can refine this dimensionless transport measure to disentangle the contributions of the Lagrangian tracers that belong to the coherent sets from those of the other tracers. We therefore define a local Nusselt number along a Lagrangian trajectory  $\mathbf{X}_i(t)$  (see also refs. [36, 37])

$$\text{Nu}^L(\mathbf{X}_i(t)) = \sqrt{\text{RaPr}} u_z T \Big|_{\mathbf{X}_i(t)} - \frac{\partial T}{\partial z} \Big|_{\mathbf{X}_i(t)}. \quad (9)$$

Thus we can take averages over time windows  $\Delta t$  for those trajectories that belong to CS and RP which leads to  $\langle \text{Nu}_{CS}^L \rangle_{\Delta t}$  and  $\langle \text{Nu}_{RP}^L \rangle_{\Delta t}$ , respectively. The time intervals  $\Delta t$  for the three runs are listed in Table I. The resulting PDFs for both subsets, CS and RP, and all three Prandtl numbers are displayed in Fig. 5. First it is observed in panels

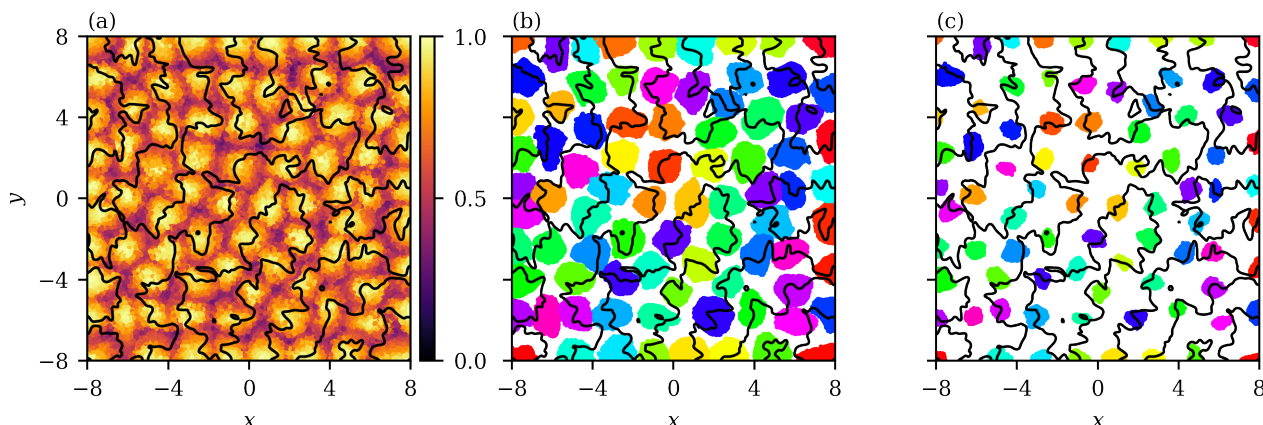


FIG. 3: Maximum likelihood of each particle to belong to a certain sparse eigenbasis approximation (SEBA) vector (a) and individual clusters (b, c) resulting from the SEBA for the same data as in Fig. 2. Each position of a Lagrangian particle corresponds to time  $t_0 + \Delta t/2$ . A separation of the features leads to the clusters shown in panel (b), while consequently not all data points belong to a feature. Here  $\zeta = 0.75$ . The colour of each data point corresponds to the detected feature thus indicating a proper separation. In panel (c) we show all Lagrangian particles corresponding to features after applying a higher threshold  $\zeta = 0.94$  to restrict them to the most inner region of the convection rolls (see also Fig. 4). Black lines indicate the isotherms ( $T$ ) = 0.5. The number of input vectors into the SEBA is 82 (see Fig.2).

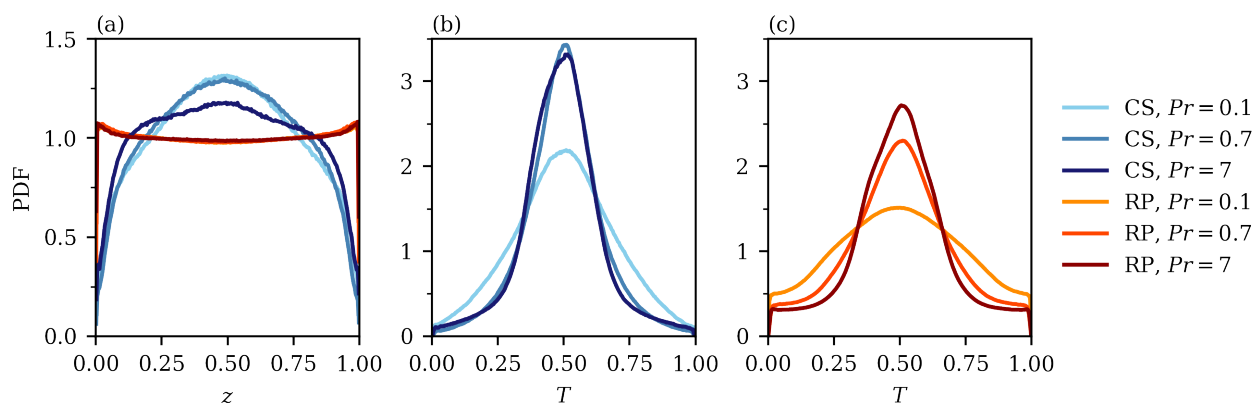


FIG. 4: Prandtl number dependence of the PDFs of tracer particles captured in the Lagrangian coherent sets (CS) and the spatial complement (RP), respectively. (a) PDF of the  $z$ -coordinate of the tracer in CS and RP. (b) PDF of the temperature  $T$  along the trajectory in CS (c) and in RP. The PDFs are computed for 10 disjoint time intervals of the evolution and arithmetically averaged subsequently. The color legend holds for all panels.

(a,b) that the support of the PDFs is smallest for the lowest Prandtl number confirming the reduced and less efficient heat transfer. Panel (c) of the same figure shows that this is in line with the coarsest thermal plumes at  $Pr = 0.1$ . The PDFs for the largest Prandtl number develop in both cases a pronounced bi-modal shape, in particular for the PDFs of  $\langle Nu_{RP}^L \rangle_{\Delta t}$ . While the peak at the positive local Nusselt number axis stands for the strong plume detachment events from both boundary layers, the peak for negative amplitude stands for impinging plumes. This effect is strongest for the largest  $Pr$  as thermal diffusion is smallest. When taking the mean values from all 6 distributions, one obtains significantly smaller values  $Nu_{CS}^L$  as  $Nu_{RP}^L$  as noted in Table I. The latter Nusselt number is very close to the original Eulerian value  $Nu^E$ .

The circumstance that Lagrangian CS act as heat transport barriers is also underlined by comparing their ratio of numerical occurrence  $\xi_p$  with the ratio of heat transported by them compared to the overall heat transport  $\xi_q$ . Our locally refined analysis of the turbulent heat transport demonstrates clearly that the core regions in which the Lagrangian trajectories are trapped for the longest time intervals contribute least.

Panels (c-e) of Fig. 5 display the Lagrangian coherent sets in instantaneous vertical cuts of the flows at the three values of  $Pr$ . The Lagrangian tracers (here we plot the end points of the corresponding trajectory segments as black dots) accumulate between the rising and falling thermal plumes which develop thinner stems with increasing Prandtl number. These plume networks would be the structures that are identified as turbulent superstructures in the Eulerian

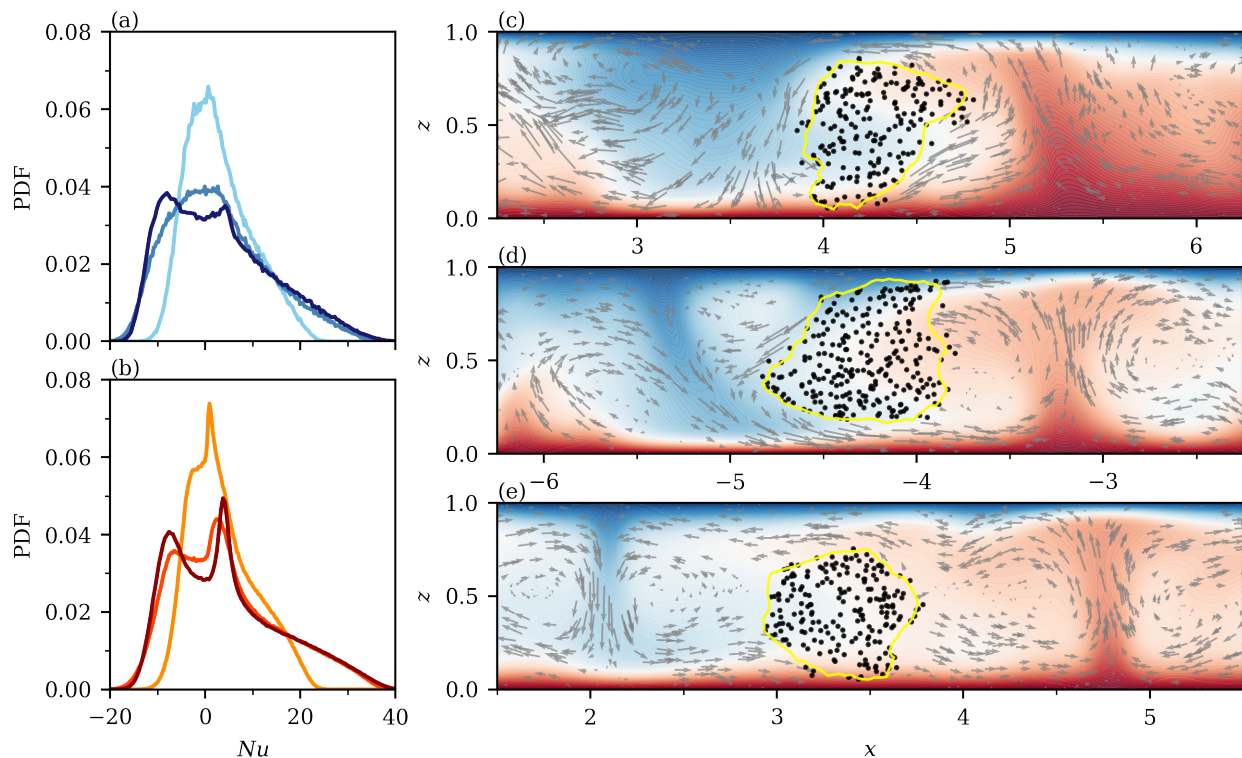


FIG. 5: Quantitative analysis and visualization of the Lagrangian barriers to heat transfer. (a) PDF of  $\langle Nu_{CS} \rangle_{\Delta t}$  whereas (b) PDF of  $\langle Nu_{RFP} \rangle_{\Delta t}$ . The color legend is exactly the same as in Fig. 4. (c-e) Data in vertical cuts with a dimensionless slice thickness of 0.2 through the RB convection layers are shown for  $Pr = 0.1$  in (c), 0.7 in (d), and 7 in (e). The isocontours of the corresponding temperature field that is averaged over  $\Delta t$  is shown as colored background. We indicate the Lagrangian tracers that belong to the Lagrangian coherent set in this slice section by black dots; their position is taken at time  $t_0 + \Delta t/2$ . The yellow contour can be considered as the transport barrier surrounding this coherent set tracer cloud. It is determined as the threshold  $\rho \geq 0.6$  in all three examples with  $\rho$  the particle number density in the coherent set. The grey vectors indicate velocity projections in the plane for tracers that belong to the spatial complement of CS taken again at  $t = t_0 + \Delta t/2$ .

frame of reference. The yellow lines mark the manifolds (cuts through closed surfaces) that surround the coherent sets in the three cases. They appear to be nearly elliptic and thus characterized by a small surface-to-volume ratio. These boundaries could thus be considered as the corresponding Lagrangian Coherent Structures [2].

## V. SUMMARY AND OUTLOOK

We have identified the Lagrangian coherent sets in three-dimensional turbulent Rayleigh-Bénard convection flows by means of clusters of massless tracer particles which are advected together with the time-dependent turbulent flow. A combination of the diffusion map framework with the subsequent sparse eigenbasis approximation led to a significantly improved identification of the coherent sets in comparison to our previous analysis in [13]. The majority of the clusters coincides with the isocontour of  $\langle T \rangle_{\Delta t} = 0.5$  which indicates an accumulation between the spatial regions of strong up- or downwelling motions – the latter of which would be identified as the significant patterns in an Eulerian analysis of the flow. This accumulation was subsequently confirmed by a statistical analysis of more than half a million Lagrangian trajectories in the RBC flow. The trajectory segments that are trapped for longer time intervals between the up- and downwelling regions are finally identified as the set that contributes least to the heat transfer. We demonstrated that the mean of the local Nusselt number  $Nu_{CS}^L$  which can be assigned to this subset is reduced to approximately 2/3rd of the global mean  $Nu^E$  in all three cases. We can thus clearly identify these regions as transport barriers.

It is clear that these trajectories are not trapped for arbitrary long time intervals inside the Lagrangian coherent sets. Individual tracer particles will join the sets, which we illustrated in panels (c-e) in Fig. 5, other will leave the moving set. Also an increase of the time interval  $\Delta t$  will cause a shrinking of the set in space. A similar trend can be observed in Neamtu-Halic et al. [38] for three-dimensional stably stratified flows or in Haller et al. [39] for turbulent channel flows where Lagrangian coherent structures – the two-dimensional manifolds that surround the Lagrangian coherent sets – have been identified. For the present approach, this suggests to apply evolutionary cluster algorithms

which would introduce a memory in time into the coherent set identification. These studies are currently underway and will be reported elsewhere. Finally, we want to mention that network analyses have been recently applied in several other turbulent flows to connect coherent structures and statistical flow properties (such as the appearance of extreme events) in reduced models which provide a further direction to extend our present work [40].

### Acknowledgments

The work of PPV and CS is supported by the Deutsche Forschungsgemeinschaft within the Priority Programme DFG-SPP 1881 on Turbulent Superstructures. Computing resources at the Jülich Supercomputing Centre by grant HIL12 of the John von Neumann Institute for Computing (NIC) are acknowledged. We thank Anna Klünker and Gary Froyland for helpful comments.

- 
- [1] M. R. Allshouse and T. Peacock, Lagrangian based methods for coherent structure detection, *Chaos* **25**, 097617 (2015).
  - [2] G. Haller, Lagrangian coherent structures, *Ann. Rev. Fluid Mech.* **47**, 137 (2015).
  - [3] A. Hadjighasem, M. Farazmand, D. Blazevski, G. Froyland, and G. Haller, A critical comparison of Lagrangian methods for coherent structure detection, *Chaos* **27**, 053104 (2017).
  - [4] G. Froyland, S. Lloyd, and N. Santitissadeekorn, Coherent sets for nonautonomous dynamical systems, *Physica D*, 239 (2010).
  - [5] G. Froyland, An analytic framework for identifying finite-time coherent sets in time-dependent dynamical systems, *Physica D* **250**, 1 (2013).
  - [6] D. Karrasch and J. Keller, A geometric heat-flow theory of Lagrangian coherent structures, *J. Nonlinear Sci.* **30**, 1849 (2020).
  - [7] G. Froyland and K. Padberg-Gehle, A rough-and-ready cluster-based approach for extracting finite-time coherent sets from sparse and incomplete trajectory data, *Chaos* **25**, 087406 (2015).
  - [8] A. Hadjighasem, D. Karrasch, H. Teramoto, and G. Haller, Spectral-clustering approach to Lagrangian vortex detection, *Phys. Rev. E* **93**, 063107 (2016).
  - [9] R. Banisch and P. Koltai, Understanding the geometry of transport: Diffusion maps for Lagrangian trajectory data unravel coherent sets, *Chaos* **27**, 035804 (2017).
  - [10] K. L. Schlueter-Kuck and J. O. Dabiri, Coherent structure colouring: identification of coherent structures from sparse data using graph theory, *J. Fluid Mech.* **811**, 468 (2017).
  - [11] K. Padberg-Gehle and C. Schneide, Network-based study of Lagrangian transport and mixing, *Nonlin. Processes Geophys.* **24**, 661 (2017).
  - [12] G. Froyland and O. Junge, Robust FEM-based extraction of finite-time coherent sets using scattered, sparse, and incomplete trajectories, *SIAM J. Appl. Dyn. Sys.* (2018).
  - [13] C. Schneide, A. Pandey, K. Padberg-Gehle, and J. Schumacher, Probing turbulent superstructures in Rayleigh-Bénard convection by Lagrangian trajectory clusters, *Phys. Rev. Fluids* **3**, 113501 (2018).
  - [14] C. Schneide, M. Stahn, A. Pandey, O. Junge, P. Koltai, K. Padberg-Gehle, and J. Schumacher, Lagrangian coherent sets in turbulent Rayleigh-Bénard convection, *Phys. Rev. E* **100**, 053103 (2019).
  - [15] A. Klünker, C. Schneide, G. Froyland, J. Schumacher, and K. Padberg-Gehle, Set-oriented finite-element study of coherent behaviour in Rayleigh-Bénard convection, In: Junge O., Schütze O., Froyland G., Ober-Blöbaum S., Padberg-Gehle K. (eds) *Advances in Dynamics, Optimization and Computation. SON 2020. Studies in Systems, Decision and Control*, vol 304. Springer, Cham, pp. 86–108 (2020).
  - [16] G. Ahlers, S. Grossmann, and D. Lohse, Heat transfer and large scale dynamics in turbulent Rayleigh-Bénard convection, *Rev. Mod. Phys.* **81**, 503 (2009).
  - [17] F. Chillà and J. Schumacher, New perspectives in turbulent Rayleigh-Bénard convection, *Eur. Phys. J. E* **35**, 58 (2012).
  - [18] B. Stevens, Atmospheric moist convection, *Annu. Rev. Earth Planet. Sci.* **33**, 605 (2005).
  - [19] J. Schumacher and K. R. Sreenivasan, Colloquium: Unusual dynamics of convection in the Sun, *Rev. Mod. Phys.* **92**, 041001 (2020).
  - [20] D. H. Kelley and T. Weier, Fluid mechanics of liquid metal batteries, *Appl. Mech. Rev.* **70**, 020801 (2018).
  - [21] R. R. Coifman, S. Lafon, A. B. Lee, M. Maggioni, B. Nadler, F. Warner, and S. W. Zucker, Geometric diffusions as a tool for harmonic analysis and structure definition of data: Diffusion maps, *Proc. Natl. Acad. Sci. USA* **102**, 7426 (2005).
  - [22] R. R. Coifman and S. Lafon, Diffusion maps, *Appl. Comput. Harmon. Anal.* **21**, 6 (2006).
  - [23] G. Froyland, C. P. Rock, and K. Sakellariou, Sparse eigenbasis approximation: Multiple feature extraction across spatiotemporal scales with application to coherent set identification, *Commun. Nonlinear Sci. Numer. Simulat.* **77**, 81 (2019).
  - [24] P. F. Fischer, An overlapping Schwarz method for spectral element solution of the incompressible Navier-Stokes equations, *J. Comp. Phys.* **133**, 84 (1997).
  - [25] J. D. Scheel, M. S. Emran, and J. Schumacher, Resolving the fine-scale structure in turbulent Rayleigh-Bénard convection, *New J. Phys.* **15**, 113063 (2013).
  - [26] R. J. A. M. Stevens, A. Blass, X. Zhu, R. Verzicco, and D. Lohse, Turbulent thermal superstructures in Rayleigh-Bénard convection, *Phys. Rev. Fluids* **3**, 041501(R) (2018).
  - [27] A. Pandey, J. D. Scheel, and J. Schumacher, Turbulent superstructures in Rayleigh-Bénard convection, *Nat. Commun.* **9**, 2118 (2018).

- [28] G. Green, D. G. Vlaykov, J. P. Mellado, and M. Wilczek, Resolved energy budget of superstructures in Rayleigh–Bénard convection, *J. Fluid Mech.* **887**, A21 (2020).
- [29] D. Krug, D. Lohse, and R. J. A. M. Stevens, Coherence of temperature and velocity superstructures in turbulent Rayleigh–Bénard flow, *J. Fluid Mech.* **887**, A2 (2020).
- [30] P. P. Vieweg, J. D. Scheel, and J. Schumacher, Supergranule aggregation for constant heat flux-driven turbulent convection, arXiv:2010.13383 (2020).
- [31] A. Klünker, C. Schneide, A. Pandey, K. Padberg-Gehle, and J. Schumacher, Lagrangian perspectives on turbulent superstructures in Rayleigh–Bénard convection, *Proc. Appl. Math. Mech.* **19**, 201900201 (2019).
- [32] P. Koltai, and S. Weiss, Diffusion maps embedding and transition matrix analysis of the large-scale flow structure in turbulent Rayleigh–Bénard convection, *Nonlinearity* **33**, 1723 (2020).
- [33] J. de la Porte, B. M. Herbst, W. Hereman, and S. J. van der Walt, An Introduction to Diffusion Maps, Proceedings of the Nineteenth Annual Symposium of the Pattern Recognition Association of South Africa, pp. 15–26 (2008).
- [34] J. Shi, and J. Malik, Normalized cuts and image segmentation, *IEEE Trans. Pattern Anal. Mach. Intell.* **22**, 88 (2000).
- [35] Y. Chi, X. Song, D. Zhou, K. Hino, and B. Tseng, Evolutionary spectral clustering by incorporating temporal smoothness, KDD '07: Proceedings of the 13th ACM SIGKDD international conference on Knowledge discovery and data mining, pp. 153–162 (2007).
- [36] Y. Gasteuil, W. L. Shew, M. Gibert, F. Chillá, B. Castaing, and J.-F. Pinton, Lagrangian temperature, velocity, and local heat flux measurement in Rayleigh–Bénard convection, *Phys. Rev. Lett.* **99**, 234302 (2007).
- [37] J. Schumacher, Lagrangian dispersion and heat transport in convective turbulence, *Phys. Rev. Lett.* **100**, 134502 (2008).
- [38] M. M. Neamtu-Halic, D. Krug, G. Haller, and M. Holzner, Lagrangian coherent structures and entrainment near the turbulent/non-turbulent interface of a gravity current, *J. Fluid Mech.* **877**, 824 (2019).
- [39] G. Haller, S. Katsanoulis, M. Holzner, B. Frohnapfel, and D. Gatti, Objective barriers to the transport of dynamically active vector fields, *J. Fluid Mech.* **905**, A17 (2020).
- [40] G. Iacobello, L. Ridolfi, and S. Scarsoglio, A review on turbulent and vortical flow analyses via complex networks, *Physica A* **563**, 125476 (2021).